

In-situ Observation of Interfacial Debonding between a Single Carbon Fiber and Epoxy Matrix by Synchrotron Radiation X-ray Nano-Imaging

Kosuke Takahashi (✉ ktakahashi@eng.hokudai.ac.jp)

Hokkaido University

Takuma Matsuo

Hokkaido University

Wataru Sato

Hokkaido University

Ryosuke Shoya

Hokkaido University

Takashi Nakamura

Hokkaido University

Akihisa Takeuchi

Japan Synchrotron Radiation Research Institute

Masayuki Uesugi

Japan Synchrotron Radiation Research Institute

Kentaro Uesugi

Japan Synchrotron Radiation Research Institute

Research Article

Keywords:

Posted Date: February 10th, 2022

DOI: <https://doi.org/10.21203/rs.3.rs-1314626/v1>

License:   This work is licensed under a Creative Commons Attribution 4.0 International License.

[Read Full License](#)

Abstract

Although the initial stage of fatigue failure accounts for failure in mechanical structures, this has not been thoroughly clarified for Carbon Fiber Reinforced Plastics (CFRPs), thereby prompting the need to develop innovative fatigue tests. In this study, interfacial debonding between a single carbon fiber and the epoxy matrix was observed using synchrotron radiation (SR) X-ray computed tomography (CT). A single carbon fiber was embedded perpendicular to the loading direction in a dumbbell-shaped epoxy sample. A tabletop fatigue testing machine driven by a piezoelectric actuator was developed to apply static and cyclic loads along the beamline for the in situ observation. The SR X-ray multiscale CT imaging was conducted by switching between an absorption-contrast projection method (micro-CT) and a phase-contrast imaging type X-ray microscopic CT (nano-CT). Micro-CT had insufficient resolution in detecting interfacial debonding, whereas nano-CT clearly visualized it under a static tensile load of 30 MPa. A gradual increase in the debonding length was detected until a static load of 50 MPa with nanovoid formation along the interface. Under cyclic loading, the debonding length increase along the interface was captured under a sinusoidal stress of 8–40 MPa after 10,000 cycles, whereas it did not propagate under a stress below 30 MPa.

1. Introduction

Carbon fiber reinforced plastics (CFRPs) are innovative structural materials because of their tunable mechanical properties, and excellent specific strength and rigidity owing to their fiber orientations. However, it is difficult to assess the failure progress because of the inhomogeneity of the material, which causes complicated fracture behaviors, such as fiber breakage and delamination¹. In particular, although fatigue failure accounts for 80% of the causes of mechanical failures, the fatigue crack initiation has not been clarified for CFRP structures. Thus, fatigue tests must be conducted individually with different fiber orientations and applied stress levels, despite the huge costs of the experiments. Several failure assessments based on phenomenological approaches have been proposed^{2–5}. However, they have not been specifically related to the mechanical properties of the carbon fiber, matrix resin, and their interface. Therefore, a general mechanism of the initiation and propagation of the fatigue crack in CFRP structures should be clarified to develop a versatile evaluation method.

One key aspect of fatigue failure is the transverse crack generated in the 90° layers, where carbon fibers do not directly affect the strength in the loading direction. The generation of the transverse crack is considered to be the first process of fatigue failure because it gradually increases during the early stage of the loading cycles^{6–9}. Although transverse cracks do not immediately reduce the rigidity and strength of CFRP laminates, they eventually cause delamination along the interface between layers with different fiber orientations. Hosoi et al. proposed an estimation method for the remaining fatigue life based on the accumulation of transverse cracks in 90° layers^{10–12}. However, the prediction of the initiation of a transverse crack remains a challenge because it strongly depends on the stacking sequence of the laminates.

The origin of transverse crack has been focused on the interfacial debonding between the carbon fiber and matrix resin¹³, as shown in Fig. 1. The scanning electron microscope observation at the site of the transverse crack implies that it propagates along the interface of the carbon fibers, and the remaining interfacial debonding is confirmed near the transverse crack¹⁰. However, it is extremely difficult to detect the nanoscale opening gap of the interfacial debonding among the innumerable carbon fibers in the CFRP laminate before propagating to be a transverse crack owing to the small diameter of the carbon fiber, which is only 7 μm . Even though finite element analysis has been utilized to investigate the failure progress in the 90° layer considering the interfacial debonding in addition to the yielding of the matrix resin, they usually require many parameters to represent the experimental results¹⁴⁻¹⁷.

To focus on the interfacial debonding of a specific carbon fiber, a single fiber fragmentation test has been widely used to estimate the interfacial shear strength by embedding a single carbon fiber along the loading direction¹⁸⁻²⁰. The interfacial debonding in the transverse direction can be characterized by a cruciform specimen method²¹. However, the interfacial debonding initiated from the interior of the matrix resin may not correspond to those initiated from the CFRP laminates because the transverse cracks are generally initiated from the free surface. Martyniuk et al. prepared an epoxy sample embedding a relatively large single glass fiber with a diameter of 50 μm , and observed it using in situ synchrotron radiation (SR) X-ray computed tomography (CT)²². They succeeded in capturing the three-dimensional (3D) debonding behavior of the fiber from the free surface toward the interior of the sample. This implies that the interfacial debonding of a carbon fiber with a diameter of approximately 7 μm can be observed if X-ray CT can be realized with a higher magnification and resolution. The sensitivity to the difference in the densities needs to be also improved because the density of the matrix resin is closer to that of carbon fiber than that of the glass fiber.

In this study, an epoxy sample with a single carbon fiber embedded in the transverse direction was prepared to capture the interfacial debonding between the carbon fiber and epoxy matrix. Interfacial debonding was generated under static and cyclic loading, and was observed using SR X-ray CT at the large synchrotron radiation facility SPring-8 (Hyogo, Japan). To realize the in situ SR X-ray CT, a piezoelectric actuator-driven desktop fatigue testing machine was developed to apply static and cyclic loads directly along the beamline.

2. Experimental

2.1 Sample Preparation and Preliminary Experiment

The epoxy resin used in this study was composed of jER828 and the curing agent jER Cure 113 (Mitsubishi Chemical) with the weight ratio of 100:32. A relatively hard curing agent was used to minimize the viscoelastic effect during loading. They were mixed using a vacuum defoaming stirrer VDS-1 (ASONE) under a vacuum environment for 5 min and placed in a vacuum oven DRV320DB (Advantech Toyo) preheated at 80°C for 15 min to completely degas the matrix. Subsequently, a single carbon fiber

T700SC (Toray) was placed across the parallel portion of the silicon mold, as illustrated in Fig. 2. Weights of 1 g were attached to both ends to prevent fiber waviness due to the curing shrinkage of the epoxy resin. The vacuum-defoamed epoxy resin was then poured into the silicon mold. The curing cycle was carried out at 80°C for 1 h, followed by 150°C for 3 h. The surfaces of the cured samples were carefully polished with emery paper in the order of #1000, #1500, and #2000, and then mirror-finished with a liquid compound with grain sizes in the order of 7, 1, and 0.2 μm .

The tensile tests were conducted to obtain the stress–strain curve of the sample. A random speckle pattern was applied to the sample surface using an airbrush to apply the digital image correlation method for strain measurement using a digital two-dimensional correlation system VIC-2D (Laser Measurement Co., Ltd.). Tensile loading was applied to the epoxy sample without the carbon fiber at 10 $\mu\text{m/s}$ using a small tensile testing machine developed in our laboratory (Fig. 3) for the in situ observation under a digital microscope MS-300 (Asahi Kougakuki Manuf.Co.,Ltd). The yield stress (0.5% proof stress), tensile strength, and elastic modulus of the neat epoxy sample were 60.4 MPa, 106.3 MPa, and 3.12 GPa, respectively.

The tensile stress required to cause interfacial debonding between the carbon fiber and epoxy resin was investigated by the stepwise increase of the tensile load under repeated loading and unloading. The same tensile testing machine and microscope were used to observe a single carbon fiber embedded in the epoxy sample. The sample was loaded to 10 MPa and unloaded to 5 MPa at a tensile velocity of 10 $\mu\text{m/s}$. The sample was again loaded at 20 MPa and unloaded to 5 MPa. The same process was repeated by increasing the maximum load to 10 MPa until fracture.

The stress–displacement curve obtained from the loading–unloading test is shown in Fig. 4(a). The vertical axis represents the nominal stress obtained by dividing the tensile load by the cross-sectional area, and the horizontal axis represents the displacement between the grips. The observed image around the carbon fiber at loads of 40 MPa, 80 MPa, and fracture are shown in Fig. 4(b). The loading and unloading curves almost overlapped until the load of 50 MPa; however, a slight hysteresis was confirmed during unloading from 60 MPa. A large hysteresis and residual displacement were confirmed during unloading from 80 MPa. Comparing the images at 40 and 80 MPa (Fig. 4(b) and Fig. 4(c), respectively) to those before loading (Fig. 2), the dark area around the boundary of the carbon fiber became slightly thicker. However, it was difficult to confirm the initiation of interfacial debonding. The sample was fractured before reaching 90 MPa through the interface between the carbon fiber and matrix (Fig. 4(d)). Although the interfacial debonding between the single carbon fiber and epoxy resin cannot be detected by our high-magnification digital microscope, it may initiated under a load of less than 60 MPa based on the hysteresis and residual displacement of the loading–unloading process.

2.2 Synchrotron Radiation X-Ray Multiscale CT

Non-destructive inspection using SR X-ray CT has been applied to visualize matrix cracking and fiber breakage; however, existing studies are at a sub-microscale, and could not sufficiently visualize the

interfacial debonding between carbon fibers and matrix resins^{23–27}. Fig. 5(a) shows a schematic of the absorption contrast projection method called “micro-CT”²⁸. In detail, a sample is placed on a rotating stage and irradiated with monochromatic X-rays. The X-ray detected by the image detector is then converted into a visible-light image captured by a charged-coupled device or complementary metal oxide semiconductor camera with an optical lens. Therefore, the spatial resolution depends on the detector specifications.

In recent years, a phase-contrast imaging-type X-ray microscopic CT, called “nano-CT”, has been developed to further improve the spatial and density resolutions of conventional X-ray CT methods²⁹. Fig. 5(b) shows a schematic of the nano-CT system. The X-ray image transmitted through the sample is magnified by the Fresnel zone plate, which is an objective lens for X-rays, to achieve the image on the detector with higher spatial resolution. In addition, introducing the phase-contrast method emphasizes the slight differences in the density to distinguish the carbon fiber from the polymer resin^{30,31}.

At the large synchrotron radiation facility SPring-8, micro-CT and nano-CT systems are available along the beamline BL20XU. These systems can be easily switched by maintaining the sample in the rotational stage. In detail, micro-CT can be conducted first to specify the area of interest, and then switch to nano-CT to focus on the obtained area with a higher resolution. This multiscale CT system is particularly beneficial for the nondestructive inspection of tiny damages. The field of view and pixel size of the micro-CT and nano-CT systems are 1 mm² with 495 nm/pixel and 62.5 μm² with 42 nm/pixel, respectively. In this study, the X-ray energy was set to 20 keV, and the exposure time per irradiation was 0.1 s for micro-CT and 0.5 s for nano-CT. The sample was rotated from 0° to 180° in 0.1° increments during the X-ray irradiation, which took approximately 3 and 15 min for micro-CT and nano-CT, respectively.

Examples of the micro-CT and nano-CT images of a single carbon fiber embedded at the center of the epoxy sample are shown in Fig. 6(a) and (b), respectively. Almost all the cross-section of the sample was captured using micro-CT imaging. The tip of the carbon fiber was magnified by nano-CT, which corresponds to the red square region in the micro-CT image. These are the resliced views along the fiber diameter from the 3D constructed image. The slight difference in the density between the carbon fiber and epoxy resin can be distinguished by both micro-CT and nano-CT. Although the micro-CT image has insufficient resolution to detect interfacial debonding along the carbon fiber, the nano-CT image at the end of the carbon fiber clearly specifies the boundary from the epoxy resin. The image before loading confirmed that the carbon fiber and epoxy matrix are closely bonded to each other.

2.3 Piezoelectric actuator-driven tabletop fatigue testing machine

To conduct the in situ observations by SR X-ray CT under tensile loading, we developed a tabletop fatigue testing machine that also allows the application of cyclic loads on the beamline³². The number of loading cycles can be efficiently increased with the imaging process. The fatigue test used to be

conducted using a hydraulic testing machine and away from the beamline owing to the concerns in the vibration during the operation. Our testing machine allows small increments of loading cycles to capture the gradual progress of the interfacial debonding because the sample does not have to be removed and replaced from the fatigue testing machine to the beamline during CT imaging. This also has the advantages of preventing accidental damage to the sample during the replacement process and time efficiency to address the limited user time at the synchrotron facility.

The testing machine mounted on the rotation stage of the beamline is shown in Fig. 7(a), and a magnified view of the sample is shown in Fig. 7(b). The cramped sample was surrounded by an acrylic cylinder with a thickness of 2 mm through which the X-rays were transmitted. The total weight was only 2.6 kg by employing a custom-ordered piezoelectric actuator produced by Shouei System Co., Ltd. The piezoelectric elements were sufficiently stacked to realize a displacement of 300 μm . A load cell was connected to a clamp fixed to the bottom of the testing machine. The load capacity was 500 N under static conditions. As this machine was originally developed for hourglass-shape specimens, adaptors were created to fix our dumbbell-shaped plate sample.

3. Results And Discussion

3.1 Static tensile test

Micro-CT and nano-CT imaging were conducted under applied tensile loadings of 30, 40, and 50 MPa. Considering the damage to the epoxy matrix due to X-ray irradiation, samples were separately prepared for each stress condition. Fig. 8(a) shows the result of the micro-CT imaging, which is a re-sliced view observed in the same direction as that in Fig. 6(a) at a tensile load of 50 MPa. Only the image around the carbon fiber is presented. The voids were distributed randomly along the carbon fiber; however, it was difficult to specify the interfacial debonding. The volume of the carbon fiber was then extracted from the constructed 3D image using binarization. The volume of the empty space was also extracted separately and then unified with the carbon fiber, as shown in Fig. 8(b). The location and size of the voids, represented in red, can be clearly related to the carbon fiber; however, there was still no indication of interfacial debonding. Hence, micro-CT did not have sufficient imaging resolution to detect interfacial debonding.

The nano-CT images obtained under stresses of 30, 40, and 50 MPa are shown in Fig. 9(a)–(c), respectively. The re-sliced views observed from the same direction as that in Fig. 6(b) are shown on the left; the black arrow indicates the sample surface. The volume of the carbon fiber was then extracted from the 3D constructed image by binarization and unified with the empty space in the epoxy matrix (in red). The boundary of the carbon fiber was significantly clearer than that of the micro-CT images. Thus, the interfacial debonding can be distinguished as the black region along the upper and lower interfaces even under a stress of 30 MPa (Fig. 9(a) and 9(b)). The carbon fiber was debonded from the epoxy matrix only near the sample surface but was still connected to the epoxy resin without any voids. The interfacial debonding length observed under a stress of 40 MPa was slightly longer for a larger opening, as shown in

Fig. 9(c) and 9(d). Local debonding isolated from the sample surface was also observed, as indicated by the red arrows. In addition, a crack was generated from the void that were trapped during the curing process. These short debonding and the crack were found only near the sample surface within a field of view of 60 μm . When a stress of 50 MPa was applied, larger debonding was observed in the field of view, particularly along the lower interface, as shown in Fig. 9(e)–(f). From the 3D view in Fig. 9(f), the lower half of the carbon fiber was almost entirely separated from the epoxy matrix. The debonding length was shorter than the fiber diameter on the upper side and small voids were distributed along the carbon fiber. As the size and appearance of these voids were different from that in Fig. 9(c), these are said to be initiated from the boundary, which indicates the lower strength of the epoxy resin in the vicinity of the interface. In addition, the debonded surface with dimple-like texture of the epoxy matrix on the lower side exhibited void formation before debonding from the carbon fiber. These results suggest that the interfacial debonding along the carbon fiber was caused by the yielding of the epoxy resin. Further, nano-CT has sufficient resolution and magnification to detect the interfacial debonding between the carbon fiber and epoxy matrix, and void formation during the debonding process.

3.2 Fatigue test

In the fatigue test, it is necessary to conduct repeated nano-imaging using the same sample to track the propagation of the interfacial debonding; however, excessive exposure to high-energy X-rays may damage the matrix resin. Therefore, the sample was fixed at a position on the stage where the tip of the carbon fibers could be observed in the same direction as that in Fig. 6(b), and only the X-ray transmission image was obtained without rotating the sample. Thus, only one pulse of X-ray exposure was required for the imaging. A transmission image used for the construction of the 3D image from the same angle in Fig. 9(a) is shown in Fig. 10. The transmission image was not as clear as the re-sliced 3D constructed image. However, the debonding length can still be determined. Therefore, the propagation of interfacial debonding can be tracked by increasing the number of loading cycles.

Based on the results of the static tensile test, cyclic loading with a maximum stress of 30 or 40 MPa was applied. The displacement of the piezoelectric actuator was controlled such that the stress ratio $R = 0.2$. The frequency of the cyclic loading was set to 10 Hz for up to 10,000 cycles and 20 Hz thereafter. The tensile loading was paused and maintained at the mean displacement when the vicinity of the sample surface was observed by an X-ray transmission nano-CT.

Figures 11(a)–(d) show the transmission images observed under a maximum stress of 30 MPa at 1, 10,000, 30,000, and 100,000 loading cycles, respectively. Although short debonding length was observed on the upper side of the carbon fiber in Fig. 11(a), similar to that in Fig. 9(a), the debonding surface did not propagate until 100,000 loading cycles, as shown in Figures 11(b)–(d). Under a maximum stress of 40 MPa, the debonding length caused by the first cycle, shown in Fig. 11(e), was slightly longer than that in Fig. 9(b), and it did not propagate until 10,000 loading cycles, as shown in Fig. 11(f). After 30,000 loading cycles, a slight increase in debonding length was finally observed, as shown in Fig. 11(g). The debonding length continued to increase until 100,000 loading cycles, as shown in Fig. 11(h). However,

debonding was not detected on the lower side of the carbon fiber in the transmission image. As it is possible to measure the debonding lengths of the upper and lower sides on both the left and right surfaces of the sample, they were measured and summarized in Fig. 12. The debonding length on the upper side of the carbon fiber was longer on the left side, whereas that on the lower side was longer on the right side. This implies that the sample was not tensioned perfectly straight and was slightly bent. Although further improvement of the tension axis is required for a more detailed investigation, it effectively followed the debonding length by transmission nanoimaging.

4. Conclusion

In this study, dumbbell-shaped epoxy samples embedded with a single carbon fiber in the transverse direction were prepared to detect the initiation of interfacial debonding. The summary of our findings is as follows.

- Interfacial debonding was not detected in the preliminary experiment of the in situ observation under a high-magnification digital microscope but was implied to occur at a stress below 60 MPa by a hysteresis loop during unloading.
- The in situ observation under synchrotron radiation X-ray CT was realized by developing a tabletop fatigue testing machine, which allows the application of cyclic loadings on the beamline.
- Micro-CT can clearly distinguish the carbon fiber from the epoxy matrix and detect small voids distributed along the interface; however, it cannot detect interfacial debonding.
- Nano-CT successfully detected interfacial debonding, and the indication of yielding of the epoxy resin along the interface from the distribution of the nano-voids.
- Transmission nano-imaging was proposed to follow the propagation of interfacial debonding under cyclic loadings to prevent damage to the epoxy matrix due to X-ray irradiation.
- The propagation of the interfacial debonding between a carbon fiber and epoxy matrix by cyclic loading was quantitatively measured for the first time.

Declarations

Acknowledgement

This work was supported by JST, PRESTO, Japan (Grant Number JP MJPR2097). The synchrotron radiation experiments were performed at the BL20XU of SPring-8 with the approval of the Japan Synchrotron Radiation Research Institute (JASRI; Proposal No. 2020B2020).

Author contributions

K.T. provided the research idea, acquired the funding, planned the experiment, and wrote the entire manuscript; T.M., W.S., and R.S. prepared the samples, conducted the experiments, and analyzed the data.

T.N. developed the testing machine. A.T., M.U., and K.U. supported the experimental operation at SPring-8. All authors reviewed the manuscript.

Data availability statement

The data sets used and/or analyzed within the current study are available from the corresponding author on reasonable request and with approval of the research sponsor

References

1. Friedrich, K. Fractographic Analysis of Polymer Composites. *Compos. Mater. Ser.* **6**, 425–487 (1989).
2. Carraro, P. A., Maragoni, L. & Quaresimin, M. Prediction of the crack density evolution in multidirectional laminates under fatigue loadings. *Compos. Sci. Technol.* **145**, 24–39 (2017).
3. Zhao, L. *et al.* A novel interpretation of fatigue delamination growth behavior in CFRP multidirectional laminates. *Compos. Sci. Technol.* **133**, 79–88 (2016).
4. Donough, M. J., Gunnion, A. J., Orifici, A. C. & Wang, C. H. Scaling parameter for fatigue delamination growth in composites under varying load ratios. *Compos. Sci. Technol.* **120**, 39–48 (2015).
5. Khan, R., Alderliesten, R., Badshah, S. & Benedictus, R. Effect of stress ratio or mean stress on fatigue delamination growth in composites: Critical review. *Compos. Struct.* **124**, 214–227 (2015).
6. Carraro, P. A., Maragoni, L. & Quaresimin, M. Characterisation and analysis of transverse crack-induced delamination in cross-ply composite laminates under fatigue loadings. *Int. J. Fatigue* **129**, 105217 (2019).
7. Hosoi, A., Sato, N., Kusumoto, Y., Fujiwara, K. & Kawada, H. High-cycle fatigue characteristics of quasi-isotropic CFRP laminates over 108 cycles (Initiation and propagation of delamination considering interaction with transverse cracks). *Int. J. Fatigue* **32**, 29–36 (2010).
8. Wu, F. & Yao, W. X. A fatigue damage model of composite materials. *Int. J. Fatigue* **32**, 134–138 (2010).
9. Llobet, J., Maimí, P., Essa, Y. & Martin de la Escalera, F. Progressive matrix cracking in carbon/epoxy cross-ply laminates under static and fatigue loading. *Int. J. Fatigue* **119**, 330–337 (2019).
10. Hosoi, A. & Kawada, H. Fatigue Life Prediction for Transverse Crack Initiation of CFRP Cross-Ply and Quasi-Isotropic Laminates. *Mater. (Basel, Switzerland)* **11**, (2018).
11. Hosoi, A., Sakuma, S., Fujita, Y. & Kawada, H. Prediction of initiation of transverse cracks in cross-ply CFRP laminates under fatigue loading by fatigue properties of unidirectional CFRP in 90° direction. *Compos. Part A Appl. Sci. Manuf.* **68**, 398–405 (2015).
12. Hosoi, A., Takamura, K., Sato, N. & Kawada, H. Quantitative evaluation of fatigue damage growth in CFRP laminates that changes due to applied stress level. *Int. J. Fatigue* **33**, 781–787 (2011).
13. Gamstedt, E. K. & Sjögren, B. A. Micromechanisms in tension-compression fatigue of composite laminates containing transverse plies. *Compos. Sci. Technol.* **59**, 167–178 (1999).

14. Kumagai, Y., Onodera, S., Salviato, M. & Okabe, T. Multiscale analysis and experimental validation of crack initiation in quasi-isotropic laminates. *Int. J. Solids Struct.* **193–194**, 172–191 (2020).
15. Sun, Q. *et al.* Failure criteria of unidirectional carbon fiber reinforced polymer composites informed by a computational micromechanics model. *Compos. Sci. Technol.* **172**, 81–95 (2019).
16. Mantič, V. & García, I. G. Crack onset and growth at the fibre–matrix interface under a remote biaxial transverse load. Application of a coupled stress and energy criterion. *Int. J. Solids Struct.* **49**, 2273–2290 (2012).
17. Vaughan, T. J. & McCarthy, C. T. Micromechanical modelling of the transverse damage behaviour in fibre reinforced composites. *Compos. Sci. Technol.* **71**, 388–396 (2011).
18. Sørensen, B. F. Micromechanical model of the single fiber fragmentation test. *Mech. Mater.* **104**, 38–48 (2017).
19. Curtin, W. A. Exact theory of fibre fragmentation in a single-filament composite. *J. Mater. Sci.* **26**, 5239–5253 (1991).
20. Budiman, B. A., Takahashi, K., Inaba, K. & Kishimoto, K. Evaluation of interfacial strength between fiber and matrix based on cohesive zone modeling. *Compos. Part A Appl. Sci. Manuf.* **90**, 211–217 (2016).
21. Ogihara, S. & Koyanagi, J. Investigation of combined stress state failure criterion for glass fiber/epoxy interface by the cruciform specimen method. *Compos. Sci. Technol.* **70**, 143–150 (2010).
22. Martyniuk, K., Sørensen, B. F., Modregger, P. & Lauridsen, E. M. 3D in situ observations of glass fibre/matrix interfacial debonding. *Compos. Part A Appl. Sci. Manuf.* **55**, 63–73 (2013).
23. Garcea, S. C., Wang, Y. & Withers, P. J. X-ray computed tomography of polymer composites. *Compos. Sci. Technol.* **156**, 305–319 (2018).
24. Bie, B. X. *et al.* Orientation-dependent tensile deformation and damage of a T700 carbon fiber/epoxy composite: A synchrotron-based study. *Carbon N. Y.* **121**, 127–133 (2017).
25. Sencu, R. M. *et al.* Generation of micro-scale finite element models from synchrotron X-ray CT images for multidirectional carbon fibre reinforced composites. *Compos. Part A Appl. Sci. Manuf.* **91**, 85–95 (2016).
26. Garcea, S. C., Sinclair, I. & Spearing, S. M. Fibre failure assessment in carbon fibre reinforced polymers under fatigue loading by synchrotron X-ray computed tomography. *Compos. Sci. Technol.* **133**, 157–164 (2016).
27. Swolfs, Y. *et al.* Synchrotron radiation computed tomography for experimental validation of a tensile strength model for unidirectional fibre-reinforced composites. *Compos. Part A Appl. Sci. Manuf.* **77**, 106–113 (2015).
28. Takeuchi, A., Uesugi, K., Uesugi, M., Yoshinaka, F. & Nakamura. Nondestructive Multiscale X-Ray Tomography by Combining Microtomography and High-Energy Phase-Contrast Nanotomography. *Microsc. Microanal.* **24**, 108–109 (2018).

29. Takeuchi, A. & Suzuki, Y. Recent progress in synchrotron radiation 3D–4D nano-imaging based on X-ray full-field microscopy. *Microscopy* **2020**, 1–18 (2020).
30. Watanabe, T., Takeichi, Y., Niwa, Y., Hojo, M. & Kimura, M. Nanoscale in situ observations of crack initiation and propagation in carbon fiber/epoxy composites using synchrotron radiation X-ray computed tomography. *Compos. Sci. Technol.* **197**, 108244 (2020).
31. Kimura, M., Watanabe, T., Takeichi, Y. & Niwa, Y. Nanoscopic origin of cracks in carbon fibre-reinforced plastic composites. *Sci. Rep.* **9**, 1–9 (2019).
32. Ryosuke Shoya, Takuma Matsuo, Kosuke Takahashi, Nao Fujimura, Takashi Nakamura. In-situ Tensile and Fatigue Testing for Detection of Interfacial Debonding between Carbon Fibers and Epoxy Matrix by Synchrotron Radiation X-ray Nano-CT [in Japanese]. *J. Japan Soc. Compos. Mater.* **47**, 186–193 (2021).

Figures

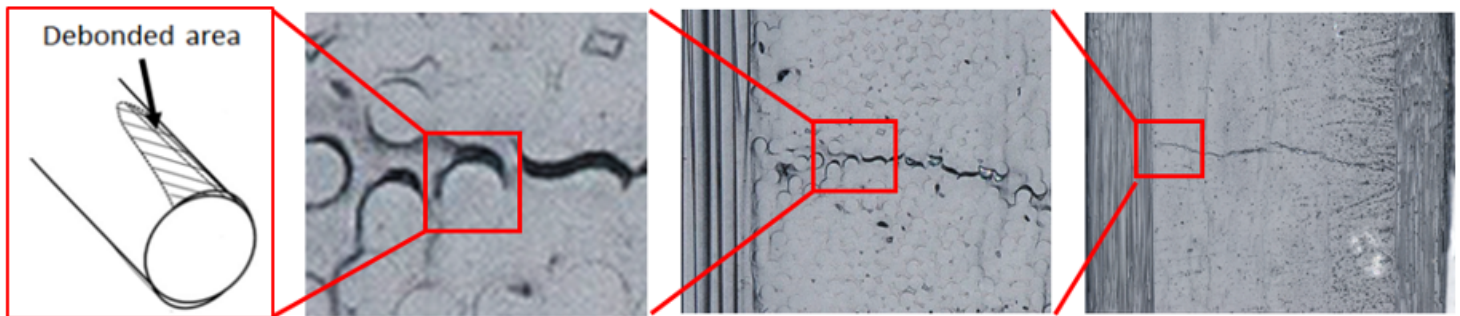


Figure 1

Schematic of a transverse crack in the 90° layer initiated from the interfacial debonding between the carbon fiber and epoxy matrix of a cross-ply laminate.

Figure 2

Sample dimensions. An observed image of a single carbon fiber under a high-magnification digital microscope.

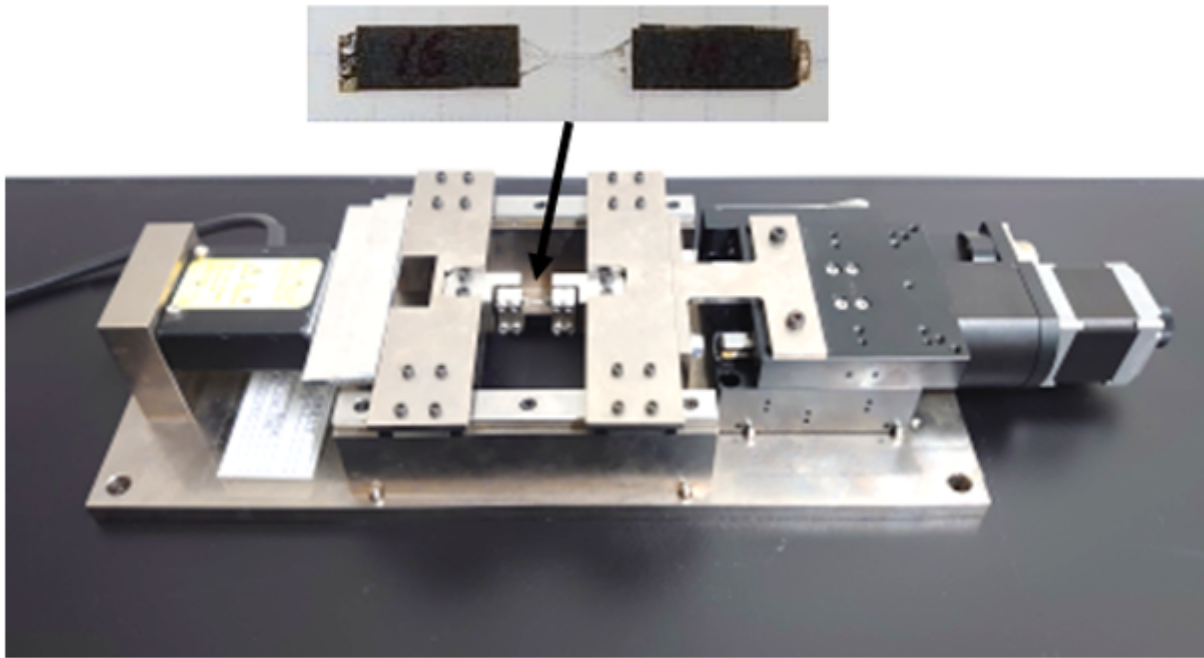


Figure 3

Tabletop tensile testing machine for the in situ observation of the sample under an optical microscope.

Figure 4

(a) Loading–unloading curve of the epoxy sample embedding a single carbon fiber. High-magnification image under a stress of (b) 40 MPa and (c) 80 MPa, and (d) at fracture.

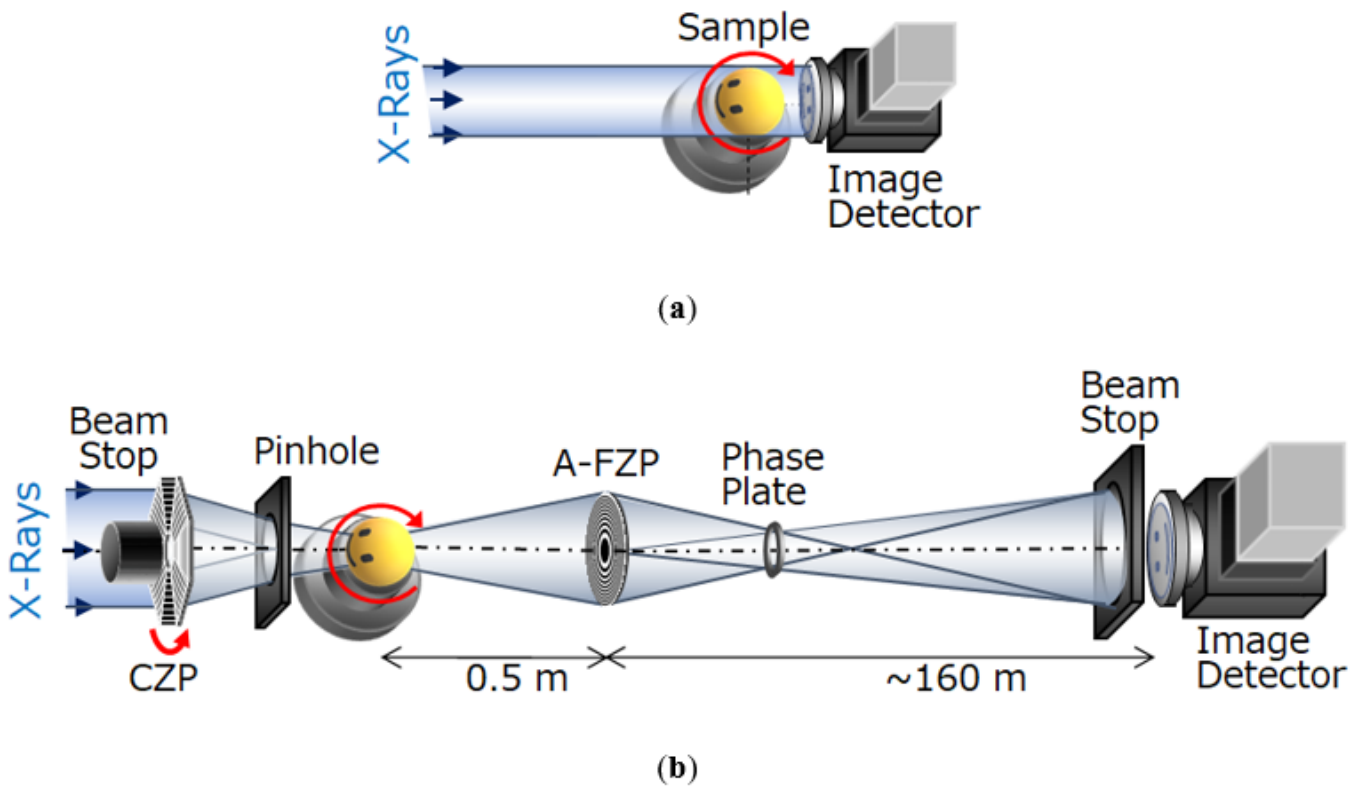
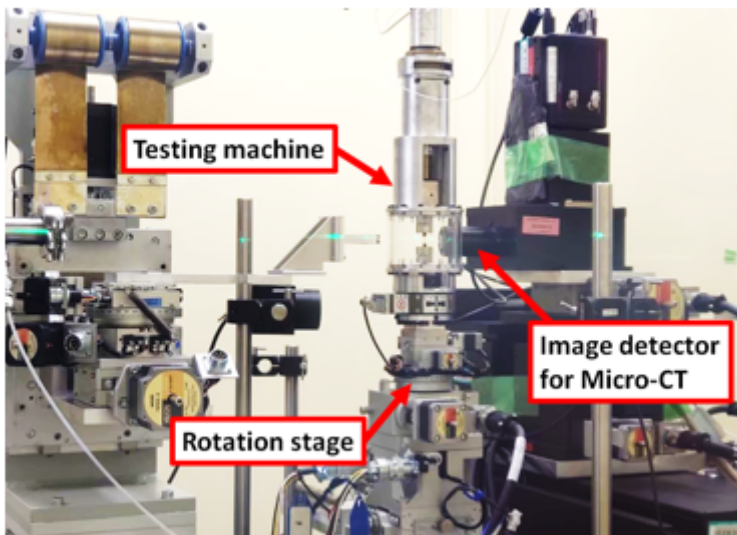


Figure 5

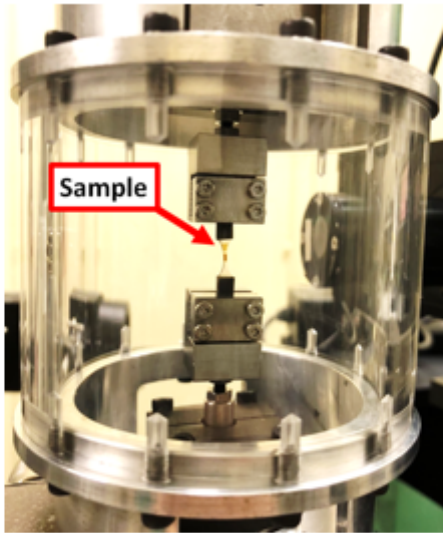
Schematic of **(a)** micro-CT and **(b)** nano-CT as synchrotron radiation multiscale X-ray CT available at beamline 20XU of SPring-8²⁸.

Figure 6

Images 3D constructed by **(a)** micro-CT and **(b)** nano-CT.



(a)



(b)

Figure 7

(a) Tabletop fatigue testing machine driven by a piezoelectric actuator installed on the beamline 20XU at SPring-8 and (b) magnified image around the cramped sample.

Figure 8

(a) Image obtained by micro-CT under a stress of 50 MPa and (b) 3D constructed image of the carbon fiber extracted by binarization. The empty spaces in the epoxy matrix are in red.

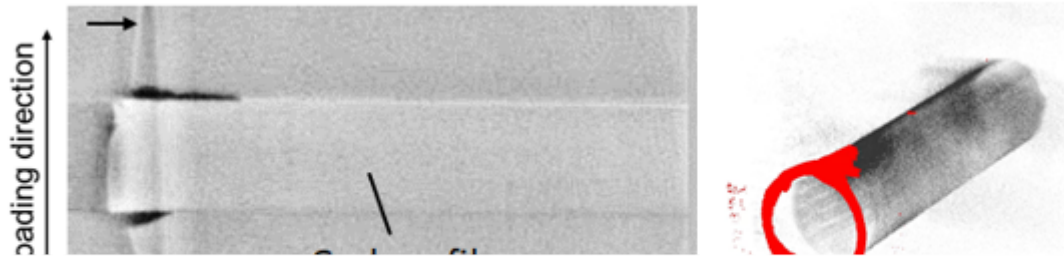


Figure 9

Images taken by nano-CT imaging under stress of **(a, b)** 30 MPa, **(c, d)** 40 MPa, and **(e, f)** 50 MPa (left) with their 3D constructed image of the carbon fiber extracted by binarization (right). The empty spaces in the epoxy matrix are in red.

Figure 10

Transmission image obtained nano-CT imaging from the same angle of Fig. 9(a).

Figure 11

Transmission nano-CT images obtained under cyclic loadings with the maximum stress of 30 and 40 MPa at (a, e) 1, (b, f) 10,000, (c, g) 30,000, and (d, h) 100,000 cycles, respectively.

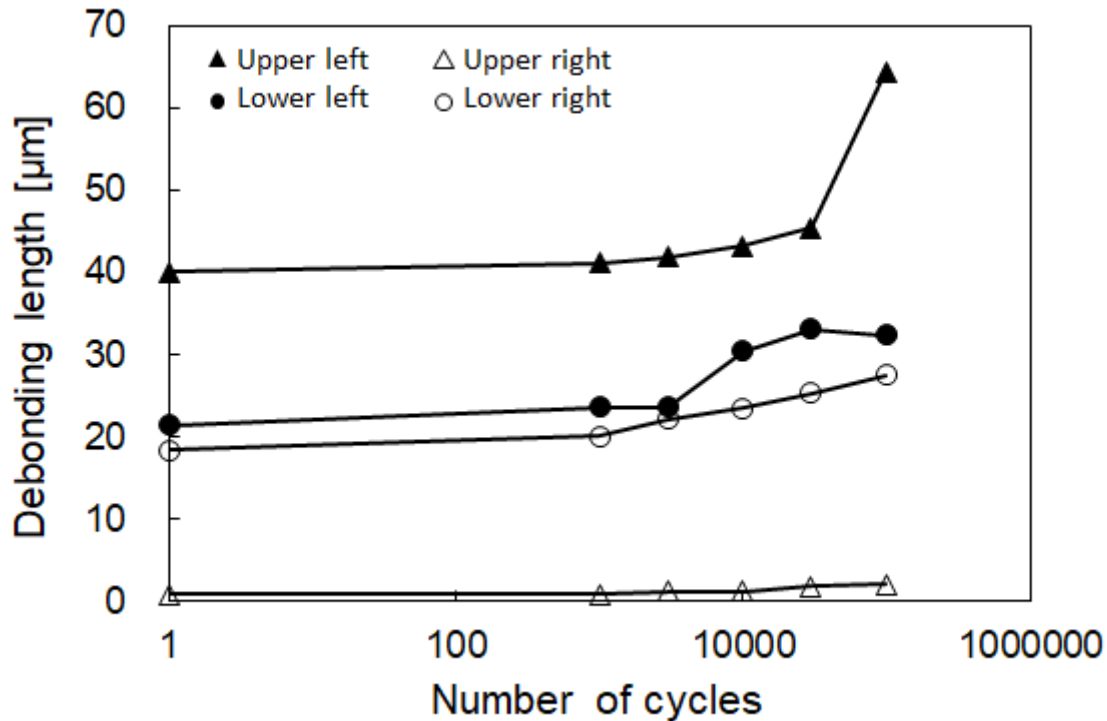


Figure 12

Measured lengths of interfacial debonding observed by transmission nano-CT imaging near the left and right sample surfaces under cyclic loadings with the maximum stress of 40 MPa.